THE JOURNAL OF PHYSICAL CHEMISTRY LETTERS
A JOURNAL OF THE AMERICAN CHEMICAL SOCIETY

pubs.acs.org/JPCL

Letter

Proximity-Induced Exchange Interaction: A New Pathway for Quantum Sensing Using Spin Centers in Hexagonal Boron Nitride

Lingnan Shen, Di Xiao,* and Ting Cao*

Cite This: *J. Phys. Chem. Lett.* 2024, 15, 4359−4366

Read Online

ACCESS | Metrics & More | Article Recommendations | Supporting Information

ABSTRACT: Defects in hexagonal boron nitride (hBN), a two-dimensional van der Waals material, have attracted a great deal of interest because of its potential in various quantum applications. Due to hBN's two-dimensional nature, the spin center in hBN can be engineered in the proximity of the target material, providing advantages over its three-dimensional counterparts, such as the nitrogen-vacancy center in diamond. Here we propose a novel quantum sensing protocol driven by exchange interaction between the spin center in hBN and the underlying magnetic substrate induced by the magnetic proximity effect. By first-principles calculation, we demonstrate that the induced exchange interaction dominates over the dipole−dipole interaction by orders of magnitude when in the proximity. The interaction remains antiferromagnetic across all stacking configurations between the spin center in hBN and the target van der Waals magnets. Additionally, we explored the scaling behavior of the exchange field as a function of the spatial separation between the spin center and the targets.

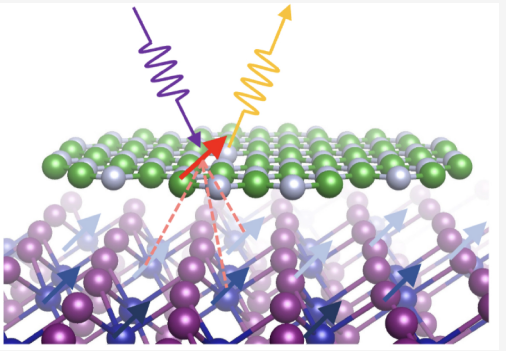

Quantum sensing based on a solid state platform has been successful in delivering high-resolution and stable measurements of various physical quantities such as temperature, pressure, strain, and magnetic, electric, and even gravitational fields.[1−4] High-precision, high-spatial resolution detection of magnetic fields is particularly important because it enables a detailed understanding of physical phenomena ranging from fundamental quantum mechanics to many intricate biological processes.[5−9] Among the candidate platforms for probing the magnetic field, color centers with a particular spin and an optical interface suitable for manipulation have been extensively investigated.[10−12] Current sensing applications predominantly rely on the Zeeman interaction between the color center spins and the small stray field generated by the sensing target. Such Zeeman splitting is in the microwave range and is usually measured by optically detected magnetic resonance (ODMR).

One widely used color center is the nitrogen-vacancy (NV) center in diamond.[5,13−15] Despite its success, the NV center suffers from several intrinsic limitations. First, high-quality NV centers are usually embedded in the diamond bulk, as it is difficult to obtain the NV center with a long coherence time near the diamond surface due to the noise from surface dangling bonds or the loss of the desirable charge state.[16,17] This bulk embedding simultaneously impedes the ability to probe the sensing target in extreme proximity for atomic resolution. Furthermore, the magnetic sensing capabilities of NV centers are constrained by their inability to detect the magnetism of underlying targets with net zero magnetic moments, like antiferromagnetic (AFM) materials, which results in a vanishing stray field signal, excluding their use as *in situ* sensors for such applications. Second, Zeeman interaction splitting is determined by the projection of the stray field to the quantization axis of the color center. If the stray field is orthogonal to the quantization axis, then there will be no signal on the ODMR spectrum. Thus, a single NV center is sensitive to only the variation of the stray field along the predetermined quantization axis. These limitations mentioned above are generic for color centers embedded in bulk semiconductors.

A material platform that supports a fundamentally new sensing paradigm could be provided by defects in hexagonal boron nitride (hBN),[18−26] a two-dimensional (2D) van der Waals (vdW) material. 2D vdW materials can be engineered into an atomically thin layer while free from dangling bonds.[27,28] This effectively resolves the two limitations we encounter with color centers in bulk semiconductors. The integration of 2D vdW materials into heterostructures facilitates the engineering of defects within a few layers from the interface with the target sample, providing an opportunity for a new paradigm of ultrasensitive, *in situ* quantum sensing.[29]

Received: March 7, 2024
Revised: April 8, 2024
Accepted: April 11, 2024
Published: April 15, 2024

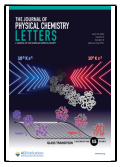

In this Letter, we propose a novel quantum sensing protocol driven by the exchange interaction between the spin center in the 2D vdW material and the target sample, demonstrated in Figure 1. Our *ab initio* calculations demonstrate a gigantic exchange interaction on the order of millielectronvolts between the negatively charged boron-vacancy (V_B^-) center and a magnetic substrate when engineered to be in the proximity of a heterostructure. Remarkably, the strength of such an exchange interaction remains robust across all stacking configurations and dominates over classical dipole−dipole or stray-field interactions. Our proposal addresses obstacles encountered with a stray-field-based sensing protocol. This work thus introduces a new exchange interaction-driven *in situ* quantum sensing scheme with the potential for ultrahigh sensitivity.

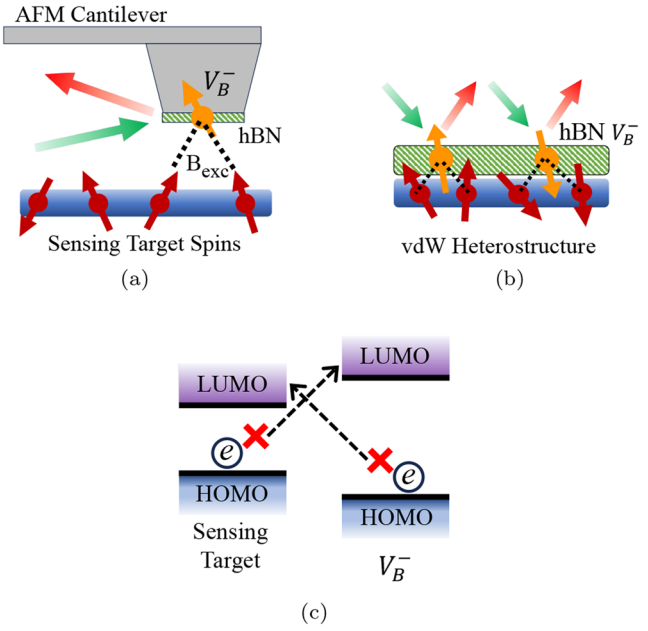

Figure 1. Schematic of quantum sensing based on proximity-induced exchange interactions. Orange and dark red arrows denote the magnetic moments of the V_B^- spin center and the sensing target (blue layer), respectively. Optical manipulation and readout of the V_B^- spin state are marked with light green and red arrows. (a) hBN layer containing a V_B^- spin center coated on an atomic force microscopy cantilever and positioned in the proximity of the sensing target. (b) vdW heterostructure formed by hBN containing ensembles of the V_B^- spin center and magnetic material, i.e., the sensing target. The dashed lines denote strong proximity-induced exchange interactions that couple the V_B^- spin centers with the local magnetic environment. (c) Schematic of the possible band alignment scenario for the V_B^- center and the sensing target. Such alignment prevents charge transfer between the V_B^- center and the sensing target, ensuring the electronic stability of the V_B^- center for quantum sensing application.

hBN hosts a variety of optically addressable defects that remain robust at room temperature and pressure.[18,22,30−35] The negatively charged boron vacancy (V_B^-) in hBN has attracted a particular level of interest due to its maturity in the fabrication process and depth of research into its electronic and optical properties. Many recent studies have demonstrated the ability to initialize, manipulate, and read out the spin state of V_B^-.[20,21,23,36,37] Since the first experimental report, the V_B^- quantum sensing application has spanned the static magnetic field, temperature, strain, pressure, and spin fluctuation.[24−26,38−40] In this work, we primarily focus on V_B^- as the quantum sensors.

We start by outlining two general design principles of quantum sensing based on proximity-induced exchange interactions. First, the quantum sensor, i.e., the spin center, has to be structurally and electronically stable. This requires no covalent or ionic chemical bonds or charge transfer between the desirable spin center and the sensing target (Figure 1c). To this end, we identified several 2D magnetic semiconductors, such as CrI_3, $CrCl_3$, and CrSBr, as the sensing target of current interests, due to their technical importance[41−45] and compatibility with the V_B^- center.

The second design principle of proximity quantum sensing is a significant exchange interaction between the quantum sensor and the target, which causes measurable changes in the electronic structures of the quantum sensors. The V_B^- center features a spin triplet ground state with a total magnetic moment of 2 μ_B. The exchange interaction will split the $m_s = 1$ and $m_s = -1$ spin states within the V_B^- ground state manifold, which could be measured by an experiment such as the optically detected magnetic resonance. Upon forming a vdW interface, we expect the exchange interaction between V_B^- and 2D magnetic semiconductors, such as CrI_3, to be comparable

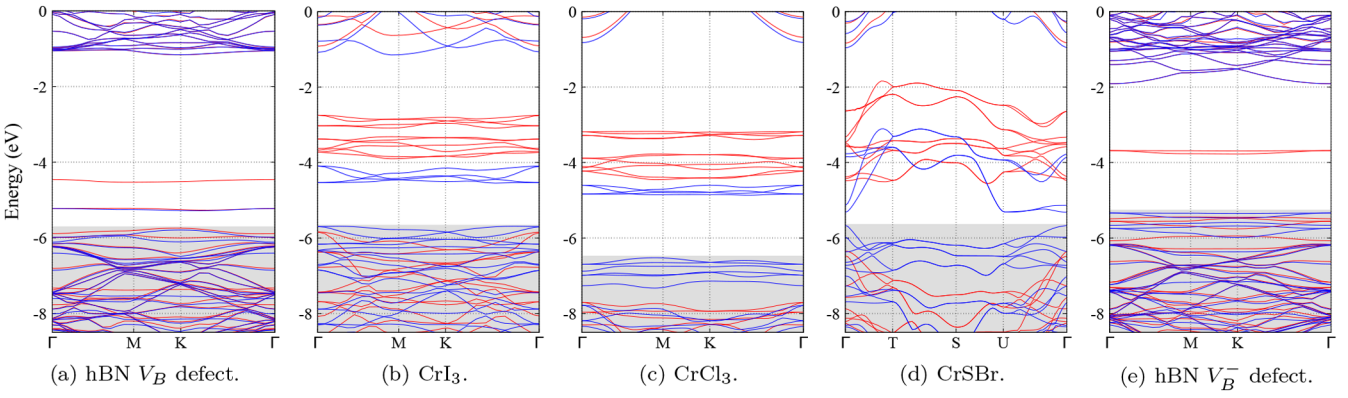

Figure 2. PBE-calculated spin-polarized band structure, showing majority spin (blue) and minority spin (red) for (a) hBN V_B, (b) CrI_3, (c) $CrCl_3$, (d) CrSBr, and (e) hBN V_B^-. Monolayer structures with a 16 Å vacuum layer are adopted. The vacuum level is set to zero for all band structures (a−d). The gray shaded regions represent the valence bands.

https://doi.org/10.1021/acs.jpclett.4c00722
J. Phys. Chem. Lett. 2024, 15, 4359−4366

in size to the pairwise exchange interactions between adjacent magnet layers. In addition, the robustness of our proposed sensing scheme is ensured by the dominance of such significant exchange interaction over other interactions such as dipole−dipole interaction.

Potential experimental realizations of this novel quantum sensing protocol include the direct integration of the V_B^- spin center with an atomic force microscopy cantilever to scan the sensing target in the proximity, as shown in Figure 1a. The hBN sheets containing the V_B^- spin center could be coated on the surface of the atomic force microscopy cantilever. Alternatively, one can incorporate the V_B^- center and the sensing target into a vdW heterostructure, depicted in Figure 1b, via existing technology such as optically detected magnetic resonance (ODMR) for the purpose of measurement. The inherent 2D nature adds extra flexibility to the experimental setup, allowing for the adaptation of the hBN sheet onto various surfaces.

Because the V_B^- center is negatively charged, electron transfer between the V_B^- center and the sensing target can lead to a change in the charge state and eventually the instability of the spin center. To satisfy the first design principle and ensure the stability of the V_B^- center, it is imperative to avoid a type III (or broken-gap) band alignment between the sensing target and the V_B^- center. In the type III configuration, the highest occupied molecular orbital (HOMO) of the V_B^- center overlaps with or exceeds the lowest unoccupied molecular orbital (LUMO) of the sensing target, or vice versa. This would suggest an alternative electronic ground state other than the desired V_B^- state. Figure 1c shows an example of the preferred band alignment between the sensing target and the V_B^- center.

We expect the proper band alignment to serve as a baseline requirement for selecting specific candidate sensing targets. As shown in Figure 2, band structure calculations are carried out for V_B and candidate monolayer target magnets, including CrI_3, $CrCl_3$, and CrSBr. The band energies are defined relative to the vacuum level. In the case of V_B^-, the vacuum level of this stand-alone charged defect is not well-defined due to the slow $1/r$ decay of the charge's Coulomb potential. However, when V_B^- and target magnets are placed adjacent to each other, the Coulomb potential will act on both systems despite a small decrease. An estimate of the band alignment may be obtained by neglecting the decrease and aligning the hBN bulk band of V_B^- (Figure 2e) to those obtained from V_B (Figure 2a). From the alignment, we find that the LUMOs of CrI_3 (Figure 2b) and $CrCl_3$ (Figure 2c) sit above the HOMO of V_B^- (Figure 2e). This ensures the charge state of V_B^- will be stable when stacked in the proximity of CrI_3 and $CrCl_3$. In contrast, the LUMO of CrSBr (Figure 2d) overlaps in energy with the HOMO of the V_B^- center, indicating charge transfer between V_B^- and CrSBr.

On the basis of this guideline, we performed direct calculations to verify the stability of the V_B^- center when placed on various 2D magnetic semiconductors that can serve as candidate sensing targets. As an example, we construct a commensurate heterostructure with a layer of hBN, containing one V_B^- center, and a monolayer of CrI_3, positioning the V_B^- center directly above a Cr atom. After full supercell lattice relaxation, the heterostructure remains flat with no discernible out-of-plane displacements or bends. The V_B^- center retained a total magnetic moment of 2 μ_B, verifying the stability of the desired V_B^- state. In addition, there is no significant alteration in the bonding environment, and the interlayer interaction remains predominantly vdW in nature.

Similar tests of stability are also performed for $CrCl_3$ and CrSBr. The heterostructure formed by the V_B^- center and monolayer $CrCl_3$ displays the same structural and electronic stability as shown in the case of CrI_3. On the contrary, the heterostructure formed by V_B^- center and monolayer CrSBr fails to maintain the atomic and electronic structure of the V_B^- state after full lattice relaxation. Our band alignment requirement successfully estimated the stability in all three test cases.

For the following study, we selected CrI_3 due to the considerable band gap it offers in the V_B^- and magnetic substrate heterostructure system, ensuring the higher electronic stability of the V_B^- charge state. We note that the self-energy corrections due to many-electron effects are not well captured in the Kohn−Sham band structures. To better describe the band alignment, we have further performed calculations using hybrid functional HSE06[46,47] because of its reasonable computational cost in the supercell. The HSE06 band alignment results (see the Supporting Information) are consistent with the DFT-PBE band alignment.

The second design principle of proximity quantum sensing requires a significant exchange interaction between the quantum sensor and target. Monolayer CrI_3 displays an out-of-plane easy-axis ferromagnetic ground state under strong intrinsic spin−orbit coupling.[48] Given the negligible spin−orbit coupling strength in hBN, the spin orientation of the V_B^- spin center should be polarized and collinear with the out-of-plane easy axis of CrI_3. The exchange interaction between CrI_3 and V_B^- can be described by a spin Hamiltonian with effective exchange field $\mathbf{B}_{exc}$

$$H = g\mu_B \mathbf{B}_{exc} \cdot \mathbf{S} \tag{1}$$

where $\mathbf{S}$ is the total electron spin − 1 operator for the V_B^- center, g is the Landé factor, and μ_B is the Bohr magneton. In our collinear calculation, $\mathbf{B}_{exc}$ remains aligned with the direction of the triplet spin center. Thus, the magnitude of such an effective exchange field can be obtained by

$$|\mathbf{B}_{exc}| = \frac{1}{g\mu_B \Delta m_s}(E_{FM} - E_{AFM}) \tag{2}$$

where E_{FM} (E_{AFM}) is the total energy of the hybrid system with FM (AFM) coupling between the V_B^- spin center and CrI_3 substrate and Δm_s is the change in the spin quantum number of V_B^-.

While the sign and magnitude of this effective exchange field can be postulated to vary, contingent on the stacking configuration between the hBN layer and CrI_3 substrate, our first-principles calculations suggest that the interaction always favors AFM coupling across all stacking configurations, regardless of the interlayer twist angle and lateral shift. To demonstrate this, we adopt an hBN flake structure hosting a V_B^- defect at the center with hydrogen termination on the edge to model the quantum sensor. The flake structure (in comparison to extended structure) allows us to fully investigate the rotational and translational degree of freedom of the stacking dependence, free from the geometry constraint of supercells.

We start by considering a monolayer hBN with V_B^- in direct contact with CrI_3 (shown in Figure 3a). As expected from our previous discussions, the V_B^- defect remains structurally and

https://doi.org/10.1021/acs.jpclett.4c00722
J. Phys. Chem. Lett. 2024, 15, 4359−4366

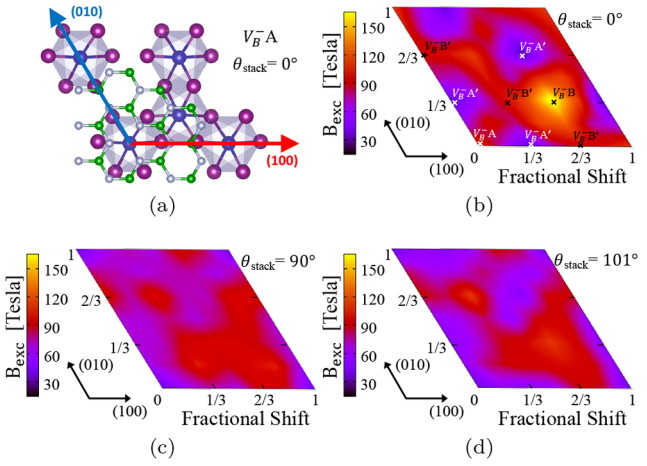

Figure 3. Dependence of effective exchange field $\mathbf{B}_{exc}$ on the interlayer stacking configuration of the hBN/CrI_3 monolayer. (a) Top view of a V_B^- defect positioned directly above a Cr atom in the A sublattice of the CrI_3 unit cell (V_B^-A stacking) that establishes the reference configuration for both interlayer rotation θ_{stack} and lateral translation. The (100) and (010) lateral shift directions are labeled with red and blue arrows, respectively. Effective exchange field $\mathbf{B}_{exc}$ calculated using the hBN flake method with (b) a θ_{stack} of 0° and (c) a θ_{stack} of 90°. (d) $\mathbf{B}_{exc}$ calculated using a periodic heterostructure with a θ_{stack} of 101°. The V_B^-B, V_B^-B′, V_B^-A′ stacking order corresponds to a fractional lateral shift of the hBN flake by approximately ($^2/_3$, $^1/_3$), ($^2/_3$, 0), ($^1/_3$, 0) with respect to the V_B^-A stacking order, respectively. The heat maps in panels b–d were drawn by interpolating neighboring data points on a 6 × 6 grid.

electronically stable upon being stacked on CrI_3. Due to the C_3 symmetry of V_B^-, the heterostructure's full interlayer twisting degree of freedom can be reduced to the range of $\theta_{stack} \in \left[0, \frac{2\pi}{3}\right]$, where θ_{stack} is the relative in-plane rotation angles between hBN and CrI_3. In total, four unique twist angles (θ_{stack}), each with a 6 × 6 grid for lateral translation in the unit cell of CrI_3, were sampled. The pattern of the effective exchange field at θ_{stack} values of 0° and 90° are shown in panels b and c, respectively, of Figure 3 (see the Supporting Information for data for θ_{stack} values of 0°, 30°, 60°, and 90°).

To verify that the findings obtained with the hBN flake method are not influenced by finite size effects, we also performed similar calculations using a periodic heterostructure composed of hBN and CrI_3. A 6 × 6 grid within the unit cell of CrI_3 is sampled, and the heat map of its effective exchange field is shown in Figure 3d. The magnitude and direction of $\mathbf{B}_{exc}$ calculated using the periodic heterostructure at 101° are close to those obtained from the hBN flake method at 90°.

The average of the effective exchange field over the sampled stacking configurations is $\bar{\mathbf{B}}_{exc} \approx 83$ T (equivalent $E_{FM} - E_{AFM} \approx 10$ meV), several orders of magnitude greater than the typical size of magnetic dipole interaction. This value varies with a standard deviation (σ_{std}) of 19 T, ranging between a minimum of 33 T and a maximum of 168 T. Interestingly, the direction of the exchange field, or the sign of $\mathbf{B}_{exc}$ from the calculations, remains unchanged throughout all stacking configurations. This contrasts with the spatially varying direction of stray fields generated by a 2D magnet several angstroms from the sample surface, as we will discuss below. Typically, the quantum sensing protocol conducted with solid state spin centers, such as the NV^- center in diamond, is performed by measuring the projected stray field to the spin center's quantization axis. A spatial variation in direction can cause the projection, and hence the interaction magnitude, to fluctuate around zero, effectively hindering sensing at the atomic level resolution. Relying on a fundamentally different mechanism, our proposed protocol showcases a unidirectional AFM exchange field that promises high sensitivity in probing the magnetism.

Next we discuss the dependence of the magnitude of $\mathbf{B}_{exc}$ on the stacking order. We selectively highlighted two equivalent stacking orders, V_B^-A′ and V_B^-B′, in Figure 3b. These particular stacking configurations were chosen for the sake of illustration because they exhibit comparable magnitudes of $\mathbf{B}_{exc}$ at all of the θ_{stack} values we calculated, suggesting a strong correlation between stacking order and $\mathbf{B}_{exc}$.

The microscopic mechanism of the interlayer coupling is AFM superexchange between the Cr atoms in CrI_3 and the V_B^- defect mediated by the I p orbitals. The Cr atom in CrI_3 is in a $3d^3$ electronic configuration with three unpaired electrons in the t_{2g} orbitals at the valence top. The V_B^- defect's magnetic moment originates from two half-filled E′ orbitals.[49] Many exchange pathways between the defect and Cr are possible. We select six main superexchange pathways, which include nearest neighbor I atoms in coordination with N atoms surrounding the V_B^- defect and two adjacent Cr atoms, with an angle ϕ in each pathway, and one such pathway is illustrated in Figure 4a.

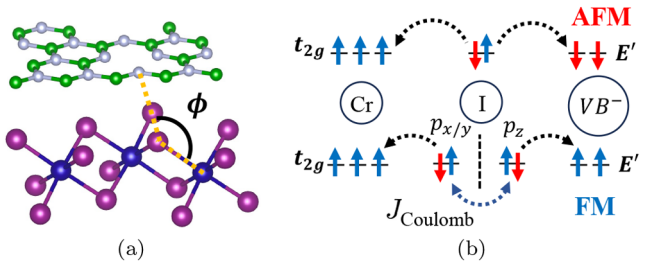

Figure 4. (a) Schematic of the interlayer superexchange pathway (orange dashed line) between the Cr atom and the V_B^- defect with the exchange pathway angle ϕ shown. (b) Schematic of angle-dependent AFM/FM interlayer superexchange.

Figure 4b demonstrates a competing exchange interaction process between the Cr atom and V_B^- defect. When the angle ϕ of the exchange pathway approaches 180°, both Cr t_{2g} orbitals and the V_B^-E′ orbitals couple to the same I p orbital, which leads to an AFM superexchange. Conversely, as ϕ nears 90°, the Cr t_{2g} orbitals and V_B^-E′ orbitals tend to couple to orthogonal I p orbitals, favoring an interlayer FM superexchange via Coulomb exchange interactions on the I atom. This competition between interlayer AFM and FM superexchange is known as the Goodenough–Kanamori rule.[50−52] We then calculated the mean value of ϕ under different stacking configurations and found that ϕ and $\mathbf{B}_{exc}$ are positively correlated, with a notable coefficient of determination (R^2) of 0.5 (see the Supporting Information for details). This strong correlation substantiates our theoretical analysis on the nature of the interlayer superexchange interaction, which favors stronger AFM coupling as ϕ increases. We do not find including the Hubbard U term has a pronounced influence on the property of this proximity-induced superexchange mechanism (see the Supporting Information for more details).

Given the significant exchange field when the V_B^- center is situated in the first hBN layer above the magnetic substrate, we

https://doi.org/10.1021/acs.jpclett.4c00722
J. Phys. Chem. Lett. 2024, 15, 4359−4366

investigate a realistic scenario in which the defect spin center is separated by pristine BN layers from the sensing targets. This scenario mimics experiments in which multiple layers of BN are often stacked atop vdW magnets. We sample stacking configurations for a bilayer hBN (in its natural AA′ stacking) flake on the CrI_3 heterostructure similar to the case of the hBN/CrI_3 monolayer, but with an additional pristine hBN layer between the V_B^- defect layer and the CrI_3 substrate.

Despite the much larger spatial separation between the V_B^- and CrI_3, we discover a large exchange field that always favors AFM coupling in the bilayer hBN/CrI_3 system. The field averages to $\overline{\mathbf{B}}_{exc} \approx 12$ T (equivalently $E_{FM} - E_{AFM} \approx 1.4$ meV), with a σ_{std} of 2.3 T and ranging between 8 and 16 T. This is a surprising finding because the exchange pathway involves an additional pristine layer of hBN with a large band gap, which introduces a barrier for the virtual hopping across the vdW gap. Figure 5 shows the magnitude of $\mathbf{B}_{exc}$ when the V_B^- defect is

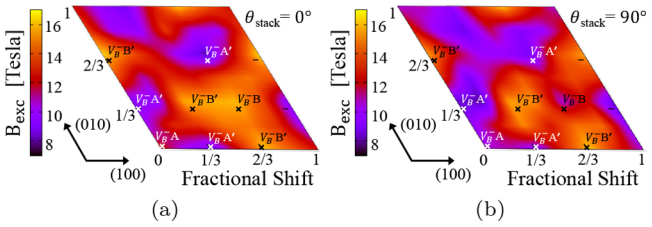

Figure 5. Effective exchange field $\mathbf{B}_{exc}$ calculated for the bilayer-hBN CrI_3 system, where there is a pristine hBN between the V_B^- layer and the CrI_3 substrate. Full space lateral translation under certain θ_{stack} interlayer relative rotations: (a) θ_{stack} = 0° and (b) θ_{stack} = 90°. Because hBN has AA′ ground state stacking, various stacking orders are preserved as marked in the heat map.

stacked onto CrI_3 at different positions (see the Supporting Information for the full set of data). The exchange field maintains a similar magnitude across varied interlayer rotations and translations, exhibiting patterns consistent with those we discovered from the first layer.

To understand the exchange interactions, we notice that with an extra pristine hBN layer, interlayer Cr−V_B^- exchange is mediated by the I p orbital and the pristine hBN's p orbital, and therefore super-superexchange in nature. Given the natural stacking configuration of the hBN layers, the vertical interlayer hopping between the orbitals of the defect and those in the pristine BN layers remains unchanged despite shifts and rotations of the bilayer relative to those of the CrI_3 substrate. It is the hybridization between the pristine hBN and the CrI_3 that determines the variation of the orbital-dependent FM and AFM exchange competition. In comparison to the super-exchange process, the super-superexchange pathway now involves a B atom directly beneath a N atom adjacent to the V_B^-, extending to an I atom, and finally connecting to the nearest neighbor Cr atom. Our first-principles results suggest that the characteristic AFM coupling, facilitated by the higher-order superexchange through the layered hBN matrix, should be preserved even as the thickness of pristine hBN between the V_B^- defect layer and CrI_3 substrate increases, because it contributes only additional vertical B−N hoppings with no stacking dependence. Therefore, our proposed quantum sensing protocol driven by such exchange interaction can be extrapolated to structures incorporating more than one layer of pristine hBN, although systematic first-principles studies are unfeasible at this moment due to the higher computational cost.

Furthermore, we analyze the dominance of exchange interaction over dipole−dipole interaction between the V_B^- spin center and the magnetic substrate as the proximity changes. Figure 6 represents exchange interaction $\mathbf{B}_{exc}$ of

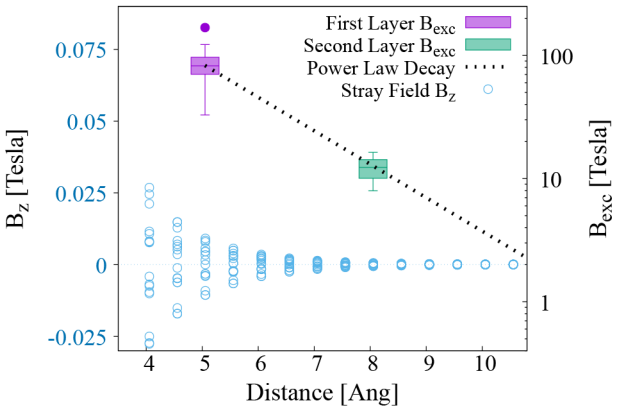

Figure 6. Quartile box plot for the magnitude of effective exchange field $\mathbf{B}_{exc}$ on a log scale containing all sampled stacking configurations from the V_B^-/CrI_3 heterostructure. The dashed black line extrapolates the power law decay of the exchange interaction strength. The stray field's $\hat{z}$ component, B_z, is shown in a linear scale (blue) calculated from uniformly sampled positions within a CrI_3 unit cell.

various stacking configurations within the first two hBN layers and compares it with the $\hat{z}$ component of stray field B_z generated by the CrI_3 substrate that is periodic in the basal plane

$$\mathbf{B}(\mathbf{r}) = \frac{\mu_0}{4\pi}\left[\frac{3\mathbf{r}(\mathbf{m}\cdot\mathbf{r})}{r^5} - \frac{\mathbf{m}}{r^3}\right] \tag{3}$$

where μ_0 is the vacuum permeability and $\mathbf{m}$ is the magnetic moment of Cr atom. The stray field, arising from each Cr ion's 3 μ_B out-of-plane magnetic moment, is 3 orders of magnitude weaker than $\mathbf{B}_{exc}$ at close proximity. Moreover, while $\mathbf{B}_{exc}$ remains robustly AFM, B_z exhibits spatial variations in sign, evident from its fluctuations around zero in Figure 6.

The robust magnetic proximity effect in the presence of additional hBN layers suggests that the exchange interaction can dominate over a dipole field even at a larger distance. As the exchange interaction depends on the overlap of the electronic wave function or hopping process, its magnitude should exhibit a power law decay as the distance or pathways become longer. Based on the decay rate from the first to second layer of hBN, we anticipate that $\mathbf{B}_{exc}$ will reach the order of 0.1 mT at the seventh layer, thereby still maintaining its dominance over the stray field for the spin center embedded in the three-dimensional structure.

In this study, we introduce a novel quantum sensing scheme driven by the exchange interaction induced by the proximity between the spin center and magnetic sensing target. The practical implementation of this principle was explored utilizing the V_B^- spin center in hBN proximate to a CrI_3 magnetic substrate, employing *ab initio* methods. Our calculation revealed a unidirectional and robust AFM exchange interaction between V_B^- and CrI_3. The exchange field is estimated to dominate the magnetic dipole field with up to

https://doi.org/10.1021/acs.jpclett.4c00722
J. Phys. Chem. Lett. 2024, 15, 4359−4366

seven layers of pristine hBN between the spin center and the magnet.

As controlled generation of the V_B^- defect at different depths and positions has been experimentally demonstrated,[32,53] our proposed proximity-induced exchange interaction-driven quantum sensing protocol can be readily realized using a hBN-coated cantilever or in a fabricated heterostructure device. The principles established from the V_B^- and CrI_3 case may be applied to other optically active spin defects in 2D materials, such as WS_2.[54] On the other hand, the V_B^- defect may also be applied to investigate magnetic materials with zero net magnetization, such as AFM materials. This is because the exchange interaction is primarily dominated by the direct or indirect overlap of electronic wave functions between quantum sensors and sensing targets, and the V_B^- defect strongly couples to magnetic ions or layers in its immediate proximity, rather than the total dipole field. This study thereby pioneers an ultrasensitive *in situ* quantum sensing model driven by proximity-induced exchange interaction between the quantum sensor and target, which may overcome intrinsic limitations of stray-field sensing.

METHODS

All *ab initio* calculations (except those specifically noted) were performed by using Density Functional Theory (DFT), with the Perdew–Burke–Ernzerhof (PBE)[55] functional for electron exchange and correlation potentials, as implemented in the VASP code.[56] We employed the projector-augmented wave (PAW)[57] method for electron–ion interaction and an energy cutoff of 520 eV for the wave function. Atomic coordinates are relaxed until forces on an atom are <0.01 eV/Å, and the total energy was converged to be within 10^{-6} eV. van der Waals interactions are included in the DFT-D2 method.[58] Moreover, a 16 Å vacuum layer is adopted to avoid interactions between the repeating images.

For the band alignment calculation, a 5 × 5 hBN supercell containing one boron vacancy was used, with a hBN lattice constant of 2.51 Å and Γ-centered 6 × 6 × 1 k-point sampling. The monolayer unit cell of CrI_3 and $CrCl_3$ was used with lattice constants of 7.01 and 5.97 Å, respectively, with a Γ-centered 9 × 9 × 1 k-point sampling for both. We use a monolayer unit cell of CrSBr with lattice constants a = 3.51 Å and b = 4.71 Å with Γ-centered 12 × 9 × 1 k-point sampling.

For the effective exchange-field calculation, we use a circular flake structure with 41 B and 42 N atoms, containing one boron vacancy in the center and a hydrogen termination on the edge. The underlying substrate contains a 4 × 4 CrI_3 unit cell in each periodic unit. We performed Γ only k-point calculation. The alternative periodic supercell of the hBN and CrI_3 heterostructure is formed by a layer of 16-hBN unit cell on 4-CrI_3 unit cell with Γ-centered 3 × 3 × 1 k-point sampling.

ASSOCIATED CONTENT

Supporting Information

The Supporting Information is available free of charge at https://pubs.acs.org/doi/10.1021/acs.jpclett.4c00722.

HSE06 band alignment, formation energy heat map, correlation between exchange pathway angle ϕ and effective exchange field $\mathbf{B}_{exc}$, influence of the correlation effect on exchange interaction, POSCAR for VASP input, and raw data for the effective exchange field (PDF)

Transparent Peer Review report available (PDF)

AUTHOR INFORMATION

Corresponding Authors

Di Xiao − *Department of Materials Science & Engineering, University of Washington, Seattle, Washington 98195-2120, United States; Department of Physics, University of Washington, Seattle, Washington 98195-1560, United States; Pacific Northwest National Laboratory, Richland, Washington 99354, United States*; Email: dixiao@uw.edu

Ting Cao − *Department of Materials Science & Engineering, University of Washington, Seattle, Washington 98195-2120, United States*; orcid.org/0000-0003-1300-6084; Email: tingcao@uw.edu

Author

Lingnan Shen − *Department of Physics, University of Washington, Seattle, Washington 98195-1560, United States*; orcid.org/0009-0004-3950-6102

Complete contact information is available at: https://pubs.acs.org/10.1021/acs.jpclett.4c00722

Notes

The authors declare no competing financial interest.

ACKNOWLEDGMENTS

The authors thank Zeeshawn Kazi, Christian Pederson, Vasileios Niaouris, and Kai-Mei Fu for insightful discussions. The theoretical framework of quantum sensing in the proximity is supported by the U.S. Department of Energy, Office of Science, National Quantum Information Science Research Centers, Co-design Center for Quantum Advantage (C2QA), under Contract DE-SC0012704. The first-principles investigation of magnetism and exchange coupling is based upon work supported by the National Science Foundation under Grant DMR-2339995. This work was facilitated through the use of advanced computational, storage, and networking infrastructure provided by the Hyak supercomputer system and funded by the University of Washington Molecular Engineering Materials Center at the University of Washington (NSF MRSEC DMR-2308979). This material is based in part upon work supported by the State of Washington through the University of Washington Clean Energy Institute.

REFERENCES

(1) Degen, C.; Reinhard, F.; Cappellaro, P. Quantum sensing. *Rev. Mod. Phys.* **2017**, *89*, 035002.

(2) Schirhagl, R.; Chang, K.; Loretz, M.; Degen, C. L. Nitrogen-Vacancy Centers in Diamond: Nanoscale Sensors for Physics and Biology. *Annu. Rev. Phys. Chem.* **2014**, *65*, 83−105.

(3) Casola, F.; Van Der Sar, T.; Yacoby, A. Probing condensed matter physics with magnetometry based on nitrogen-vacancy centres in diamond. *Nat. Rev. Mater.* **2018**, *3*, 17088.

(4) Wolfowicz, G.; Heremans, F. J.; Anderson, C. P.; Kanai, S.; Seo, H.; Gali, A.; Galli, G.; Awschalom, D. D. Quantum guidelines for solid-state spin defects. *Nature Reviews Materials* **2021**, *6*, 906−925.

(5) Song, T.; Sun, Q.-C.; Anderson, E.; Wang, C.; Qian, J.; Taniguchi, T.; Watanabe, K.; McGuire, M. A.; Stöhr, R.; Xiao, D.; Cao, T.; Wrachtrup, J.; Xu, X. Direct visualization of magnetic domains and moiré magnetism in twisted 2D magnets. *Science* **2021**, *374*, 1140−1144.

(6) Finco, A.; et al. Imaging non-collinear antiferromagnetic textures via single spin relaxometry. *Nat. Commun.* **2021**, *12*, 767.

(7) Huang, M.; et al. Revealing intrinsic domains and fluctuations of moiré magnetism by a wide-field quantum microscope. *Nat. Commun.* **2023**, *14*, 5259.
(8) Barry, J. F.; Turner, M. J.; Schloss, J. M.; Glenn, D. R.; Song, Y.; Lukin, M. D.; Park, H.; Walsworth, R. L. Optical magnetic detection of single-neuron action potentials using quantum defects in diamond. *Proc. Natl. Acad. Sci. U. S. A.* **2016**, *113*, 14133−14138.
(9) Aslam, N.; Zhou, H.; Urbach, E. K.; Turner, M. J.; Walsworth, R. L.; Lukin, M. D.; Park, H. Quantum sensors for biomedical applications. *Nature Reviews Physics* **2023**, *5*, 157−169.
(10) Koehl, W. F.; Buckley, B. B.; Heremans, F. J.; Calusine, G.; Awschalom, D. D. Room temperature coherent control of defect spin qubits in silicon carbide. *Nature* **2011**, *479*, 84−87.
(11) Zhang, G.; Cheng, Y.; Chou, J.-P.; Gali, A. Material platforms for defect qubits and single-photon emitters. *Appl. Phys. Rev.* **2020**, *7*, 031308.
(12) Freysoldt, C.; Grabowski, B.; Hickel, T.; Neugebauer, J.; Kresse, G.; Janotti, A.; Van De Walle, C. G. First-principles calculations for point defects in solids. *Rev. Mod. Phys.* **2014**, *86*, 253−305.
(13) Maze, J. R.; Stanwix, P. L.; Hodges, J. S.; Hong, S.; Taylor, J. M.; Cappellaro, P.; Jiang, L.; Dutt, M. V. G.; Togan, E.; Zibrov, A. S.; Yacoby, A.; Walsworth, R. L.; Lukin, M. D. Nanoscale magnetic sensing with an individual electronic spin in diamond. *Nature* **2008**, *455*, 644−647.
(14) Kolkowitz, S.; Safira, A.; High, A. A.; Devlin, R. C.; Choi, S.; Unterreithmeier, Q. P.; Patterson, D.; Zibrov, A. S.; Manucharyan, V. E.; Park, H.; Lukin, M. D. Probing Johnson noise and ballistic transport in normal metals with a single-spin qubit. *Science* **2015**, *347*, 1129−1132.
(15) Steinert, S.; Ziem, F.; Hall, L. T.; Zappe, A.; Schweikert, M.; Götz, N.; Aird, A.; Balasubramanian, G.; Hollenberg, L.; Wrachtrup, J. Magnetic spin imaging under ambient conditions with sub-cellular resolution. *Nat. Commun.* **2013**, *4*, 1607.
(16) Romach, Y.; Müller, C.; Unden, T.; Rogers, L.; Isoda, T.; Itoh, K.; Markham, M.; Stacey, A.; Meijer, J.; Pezzagna, S.; Naydenov, B.; McGuinness, L.; Bar-Gill, N.; Jelezko, F. Spectroscopy of Surface-Induced Noise Using Shallow Spins in Diamond. *Phys. Rev. Lett.* **2015**, *114*, 017601.
(17) Bluvstein, D.; Zhang, Z.; Jayich, A. C. B. Identifying and Mitigating Charge Instabilities in Shallow Diamond Nitrogen-Vacancy Centers. *Phys. Rev. Lett.* **2019**, *122*, 076101.
(18) Attaccalite, C.; Wirtz, L.; Marini, A.; Rubio, A. Efficient Gate-tunable light-emitting device made of defective boron nitride nanotubes: from ultraviolet to the visible. *Sci. Rep.* **2013**, *3*, 2698.
(19) Durand, A.; Clua-Provost, T.; Fabre, F.; Kumar, P.; Li, J.; Edgar, J.; Udvarhelyi, P.; Gali, A.; Marie, X.; Robert, C.; Gérard, J.; Gil, B.; Cassabois, G.; Jacques, V. Optically Active Spin Defects in Few-Layer Thick Hexagonal Boron Nitride. *Phys. Rev. Lett.* **2023**, *131*, 116902.
(20) Gottscholl, A.; Diez, M.; Soltamov, V.; Kasper, C.; Sperlich, A.; Kianinia, M.; Bradac, C.; Aharonovich, I.; Dyakonov, V. Room temperature coherent control of spin defects in hexagonal boron nitride. *Sci. Adv.* **2021**, *7*, eabf3630.
(21) Gottscholl, A.; Kianinia, M.; Soltamov, V.; Orlinskii, S.; Mamin, G.; Bradac, C.; Kasper, C.; Krambrock, K.; Sperlich, A.; Toth, M.; Aharonovich, I.; Dyakonov, V. Initialization and read-out of intrinsic spin defects in a van der Waals crystal at room temperature. *Nat. Mater.* **2020**, *19*, 540−545.
(22) Chen, Y.; Quek, S. Y. Photophysical Characteristics of Boron Vacancy-Derived Defect Centers in Hexagonal Boron Nitride. *J. Phys. Chem. C* **2021**, *125*, 21791−21802.
(23) Mathur, N.; Mukherjee, A.; Gao, X.; Luo, J.; McCullian, B. A.; Li, T.; Vamivakas, A. N.; Fuchs, G. D. Excited-state spin-resonance spectroscopy of V_B^- defect centers in hexagonal boron nitride. *Nat. Commun.* **2022**, *13*, 3233.
(24) Healey, A. J.; Scholten, S. C.; Yang, T.; Scott, J. A.; Abrahams, G. J.; Robertson, I. O.; Hou, X. F.; Guo, Y. F.; Rahman, S.; Lu, Y.; Kianinia, M.; Aharonovich, I.; Tetienne, J.-P. Quantum microscopy with van der Waals heterostructures. *Nat. Phys.* **2023**, *19*, 87−91.
(25) Huang, M.; Zhou, J.; Chen, D.; Lu, H.; McLaughlin, N. J.; Li, S.; Alghamdi, M.; Djugba, D.; Shi, J.; Wang, H.; Du, C. R. Wide field imaging of van der Waals ferromagnet Fe3GeTe2 by spin defects in hexagonal boron nitride. *Nat. Commun.* **2022**, *13*, 5369.
(26) Gottscholl, A.; Diez, M.; Soltamov, V.; Kasper, C.; Krauße, D.; Sperlich, A.; Kianinia, M.; Bradac, C.; Aharonovich, I.; Dyakonov, V. Spin defects in hBN as promising temperature, pressure and magnetic field quantum sensors. *Nat. Commun.* **2021**, *12*, 4480.
(27) Dean, C. R.; Young, A. F.; Meric, I.; Lee, C.; Wang, L.; Sorgenfrei, S.; Watanabe, K.; Taniguchi, T.; Kim, P.; Shepard, K. L.; Hone, J. Boron nitride substrates for high-quality graphene electronics. *Nat. Nanotechnol.* **2010**, *5*, 722−726.
(28) Radisavljevic, B.; Radenovic, A.; Brivio, J.; Giacometti, V.; Kis, A. Single-layer MoS2 transistors. *Nat. Nanotechnol.* **2011**, *6*, 147−150.
(29) Novoselov, K. S.; Mishchenko, A.; Carvalho, A.; Castro Neto, A. H. 2D materials and van der Waals heterostructures. *Science* **2016**, *353*, aac9439.
(30) Stern, H. L.; Gu, Q.; Jarman, J.; Eizagirre Barker, S.; Mendelson, N.; Chugh, D.; Schott, S.; Tan, H. H.; Sirringhaus, H.; Aharonovich, I.; Atatüre, M. Room-temperature optically detected magnetic resonance of single defects in hexagonal boron nitride. *Nat. Commun.* **2022**, *13*, 618.
(31) Li, S.; Gali, A. Identification of an Oxygen Defect in Hexagonal Boron Nitride. *J. Phys. Chem. Lett.* **2022**, *13*, 9544−9551.
(32) Guo, N.-J.; et al. Generation of Spin Defects by Ion Implantation in Hexagonal Boron Nitride. *ACS Omega* **2022**, *7*, 1733−1739.
(33) Jin, C.; Lin, F.; Suenaga, K.; Iijima, S. Fabrication of a Freestanding Boron Nitride Single Layer and Its Defect Assignments. *Phys. Rev. Lett.* **2009**, *102*, 195505.
(34) Mendelson, N.; et al. Identifying carbon as the source of visible single-photon emission from hexagonal boron nitride. *Nat. Mater.* **2021**, *20*, 321−328.
(35) Chejanovsky, N.; Mukherjee, A.; Geng, J.; Chen, Y.-C.; Kim, Y.; Denisenko, A.; Finkler, A.; Taniguchi, T.; Watanabe, K.; Dasari, D. B. R.; Auburger, P.; Gali, A.; Smet, J. H.; Wrachtrup, J. Single-spin resonance in a van der Waals embedded paramagnetic defect. *Nat. Mater.* **2021**, *20*, 1079−1084.
(36) Liu, W.; et al. Coherent dynamics of multi-spin V_B^- center in hexagonal boron nitride. *Nat. Commun.* **2022**, *13*, 5713.
(37) Gao, X.; Vaidya, S.; Li, K.; Ju, P.; Jiang, B.; Xu, Z.; Allcca, A. E. L.; Shen, K.; Taniguchi, T.; Watanabe, K.; Bhave, S. A.; Chen, Y. P.; Ping, Y.; Li, T. Nuclear spin polarization and control in hexagonal boron nitride. *Nat. Mater.* **2022**, *21*, 1024−1028.
(38) Liu, W.; et al. Temperature-Dependent Energy-Level Shifts of Spin Defects in Hexagonal Boron Nitride. *ACS Photonics* **2021**, *8*, 1889−1895.
(39) Lyu, X.; Tan, Q.; Wu, L.; Zhang, C.; Zhang, Z.; Mu, Z.; Zúñiga-Pérez, J.; Cai, H.; Gao, W. Strain Quantum Sensing with Spin Defects in Hexagonal Boron Nitride. *Nano Lett.* **2022**, *22*, 6553−6559.
(40) Yang, T.; Mendelson, N.; Li, C.; Gottscholl, A.; Scott, J.; Kianinia, M.; Dyakonov, V.; Toth, M.; Aharonovich, I. Spin defects in hexagonal boron nitride for strain sensing on nanopillar arrays. *Nanoscale* **2022**, *14*, 5239−5244.
(41) Lu, X.; Fei, R.; Zhu, L.; Yang, L. Meron-like topological spin defects in monolayer CrCl3. *Nat. Commun.* **2020**, *11*, 4724.
(42) Huang, B.; Clark, G.; Navarro-Moratalla, E.; Klein, D. R.; Cheng, R.; Seyler, K. L.; Zhong, D.; Schmidgall, E.; McGuire, M. A.; Cobden, D. H.; Yao, W.; Xiao, D.; Jarillo-Herrero, P.; Xu, X. Layer-dependent ferromagnetism in a van der Waals crystal down to the monolayer limit. *Nature* **2017**, *546*, 270−273.
(43) Cai, X.; Song, T.; Wilson, N. P.; Clark, G.; He, M.; Zhang, X.; Taniguchi, T.; Watanabe, K.; Yao, W.; Xiao, D.; McGuire, M. A.; Cobden, D. H.; Xu, X. Atomically Thin $CrCl_3$: An In-Plane Layered Antiferromagnetic Insulator. *Nano Lett.* **2019**, *19*, 3993−3998.
(44) Lee, K.; Dismukes, A. H.; Telford, E. J.; Wiscons, R. A.; Wang, J.; Xu, X.; Nuckolls, C.; Dean, C. R.; Roy, X.; Zhu, X. Magnetic Order

https://doi.org/10.1021/acs.jpclett.4c00722
J. Phys. Chem. Lett. 2024, 15, 4359−4366

and Symmetry in the 2D Semiconductor CrSBr. *Nano Lett.* **2021**, *21*, 3511−3517.
(45) Telford, E. J.; Dismukes, A. H.; Lee, K.; Cheng, M.; Wieteska, A.; Bartholomew, A. K.; Chen, Y.; Xu, X.; Pasupathy, A. N.; Zhu, X.; Dean, C. R.; Roy, X. Layered Antiferromagnetism Induces Large Negative Magnetoresistance in the van der Waals Semiconductor CrSBr. *Adv. Mater.* **2020**, *32*, 2003240.
(46) Heyd, J.; Scuseria, G. E.; Ernzerhof, M. Hybrid functionals based on a screened Coulomb potential. *J. Chem. Phys.* **2003**, *118*, 8207−8215.
(47) Krukau, A. V.; Vydrov, O. A.; Izmaylov, A. F.; Scuseria, G. E. Influence of the exchange screening parameter on the performance of screened hybrid functionals. *J. Chem. Phys.* **2006**, *125*, 224106.
(48) Xu, C.; Feng, J.; Xiang, H.; Bellaiche, L. Interplay between Kitaev interaction and single ion anisotropy in ferromagnetic CrI3 and CrGeTe3 monolayers. *npj Comput. Mater.* **2018**, *4*, 1−6.
(49) Abdi, M.; Chou, J.-P.; Gali, A.; Plenio, M. B. Color Centers in Hexagonal Boron Nitride Monolayers: A Group Theory and Ab Initio Analysis. *ACS Photonics* **2018**, *5*, 1967−1976.
(50) Goodenough, J. B. Theory of the Role of Covalence in the Perovskite-Type Manganites [La, M(II)]MnO_3. *Phys. Rev.* **1955**, *100*, 564−573.
(51) Goodenough, J. B. An interpretation of the magnetic properties of the perovskite-type mixed crystals $La_{1-x}Sr_xCoO_{3-\lambda}$. *J. Phys. Chem. Solids* **1958**, *6*, 287−297.
(52) Kanamori, J. Superexchange interaction and symmetry properties of electron orbitals. *J. Phys. Chem. Solids* **1959**, *10*, 87−98.
(53) Gao, X.; Jiang, B.; Llacsahuanga Allcca, A. E.; Shen, K.; Sadi, M. A.; Solanki, A. B.; Ju, P.; Xu, Z.; Upadhyaya, P.; Chen, Y. P.; Bhave, S. A.; Li, T. High-Contrast Plasmonic-Enhanced Shallow Spin Defects in Hexagonal Boron Nitride for Quantum Sensing. *Nano Lett.* **2021**, *21*, 7708−7714.
(54) Li, S.; Thiering, G.; Udvarhelyi, P.; Ivády, V.; Gali, A. Carbon defect qubit in two-dimensional WS2. *Nat. Commun.* **2022**, *13*, 1210.
(55) Perdew, J. P.; Burke, K.; Ernzerhof, M. Generalized Gradient Approximation Made Simple. *Phys. Rev. Lett.* **1996**, *77*, 3865−3868.
(56) Kresse, G.; Furthmüller, J. Efficiency of ab-initio total energy calculations for metals and semiconductors using a plane-wave basis set. *Comput. Mater. Sci.* **1996**, *6*, 15−50.
(57) Kresse, G.; Joubert, D. From ultrasoft pseudopotentials to the projector augmented-wave method. *Phys. Rev. B* **1999**, *59*, 1758−1775.
(58) Grimme, S. Semiempirical GGA-type density functional constructed with a long-range dispersion correction. *J. Comput. Chem.* **2006**, *27*, 1787−1799.

https://doi.org/10.1021/acs.jpclett.4c00722
J. Phys. Chem. Lett. 2024, 15, 4359−4366